

Computational Study of Failure of Hybrid Steel Trussed Concrete Beams

Roberto Ballarini, F.ASCE¹; Lidia La Mendola²; Jia-Liang Le, A.M.ASCE³; and Alessia Monaco⁴

Abstract: This study investigates the failure behavior of hybrid steel trussed concrete beams (HSTCBs) under three-point bending through a series of finite-element (FE) simulations. The FE model employs well-established constitutive relations of concrete and steel with a simplified contact condition between the concrete and steel truss. The numerical model is compared with existing experimental data as well as a FE model that uses a more sophisticated concrete-steel interfacial model. The comparison shows that the present model is able to capture various failure mechanisms of the beam and its peak load capacity. The model is applied to investigate the behavior of a set of HSTCBs of different sizes, whose design corresponds to current industrial practice. The simulations show that, due to the lack of three-dimensional geometrical similarity, the small-size beam exhibits shear failure, whereas the large-size beam experiences flexural failure. The observed transition between different failure modes indicates the importance of employing a robust three-dimensional FE model for design extrapolation of HSTCBs across different sizes and geometries. DOI: [10.1061/\(ASCE\)ST.1943-541X.0001792](https://doi.org/10.1061/(ASCE)ST.1943-541X.0001792). © 2017 American Society of Civil Engineers.

Author keywords: Composite beam; Finite-element modeling; Fracture; Size and geometrical effects; Metal and composite structures.

Introduction

Hybrid steel trussed concrete beams (HSTCBs) represent an innovative structural solution for beams in light industry buildings and seismic-framed structures. This type of beam has been developed by the Italian construction industry over the last 50 years. In HSTCBs, a prefabricated steel truss is embedded into a cast-in-place concrete core, as shown in Fig. 1. The truss usually consists of a bottom steel plate, a system of ribbed or smooth steel bars welded together to form the diagonals of the truss, and an upper chord made of single or coupled rebars. HSTCBs could lead to a significant reduction in construction time and at the same time minimize the risk of injury because no formwork or intermediate supports are required due to the presence of the bottom steel plate and the intermittent support devices, as shown in Fig. 1. Moreover, the construction details can be controlled well without the need of in situ welding or tying. Finally, HSTCBs are able to cover a large span with a relatively small beam depth.

Since their inception a significant amount of research has been performed on different aspects of HSTCBs. For instance,

Colajanni et al. (2013) investigated the strength of welded joints, providing models for its prediction; Vincenzi and Savoia (2010) and Trentadue et al. (2011) studied the buckling of steel trusses in the operative phase preceding the concrete cast; several researchers analyzed the flexural and shear strengths of the beam (Tesser and Scotta 2013; Chisari and Amadio 2014; Monaco 2014, 2016; Campione et al. 2016; Monti and Petrone 2015; Colajanni et al. 2015b, 2016a, b); Ju et al. (2007), Amadio et al. (2011), Colajanni et al. (2015b), and Monaco (2014) investigated the behavior of beam-to-column joints and connections; and Hsu et al. (2004) and Badalamenti et al. (2010) studied the seismic behavior of HSCTBs. Tullini and Minghini (2013), Monaco (2014), and Colajanni et al. (2014, 2015a, 2016a, 2017) recently investigated the stress transfer from the bottom chord of the truss to the concrete core. Sassone and Chiorino (2005) analyzed the time-dependent creep behavior of HSCTBs.

Existing studies of the flexural and shear responses of HSCTBs have mainly dealt with experimental testing (Chisari and Amadio 2014; Monaco 2014; Monti and Petrone 2015; Colajanni et al. 2016a) and the interpretation of the test results through simplified analytical modeling (Tesser and Scotta 2013; Chisari and Amadio 2014; Monaco 2014, 2016; Campione et al. 2016; Monti and Petrone 2015; Colajanni et al. 2016b). In addition to analytical modeling of the flexural and shear resistance of HSCTBs, efforts have been devoted to developing FE methods for different beam typologies of the lower steel plate and the precast concrete base (Tesser and Scotta 2013; Chisari and Amadio 2014; Monaco 2014, 2016; Campione et al. 2016; Colajanni et al. 2015a; Monti and Petrone 2015).

Due to the complex three-dimensional (3D) geometry of HSTCBs and the nonlinear constitutive behavior of the materials and concrete-steel interface, HSTCBs can exhibit different failure modes. This makes it difficult to develop a single analytical model for predicting the failure load of HSTCBs. Therefore, computational modeling becomes an essential tool. However, few studies have been devoted to the development of efficient computational models that can capture the failure behavior of HSTCBs reasonably well and possibly be applied to the design process. This is what motivates the present work.

¹Thomas and Laura Hsu Professor and Chair, Dept. of Civil and Environmental Engineering, Cullen College of Engineering, Univ. of Houston, N127 Engineering Bldg. 1, Houston, TX 77204-4003. E-mail: rballarini@uh.edu

²Professor, Dept. of Civil, Environmental, Aerospace and Material Engineering, Univ. of Palermo, Viale delle Scienze Edificio 8, 90128 Palermo, Italy. E-mail: lidia.lamendola@unipa.it

³Associate Professor, Dept. of Civil, Environmental, and Geo-Engineering, Univ. of Minnesota, 500 Pillsbury Dr. SE, Minneapolis, MN 55455-0116. E-mail: jle@umn.edu

⁴Research Fellow, Dept. of Civil, Environmental, Aerospace and Material Engineering, Univ. of Palermo, Viale delle Scienze Edificio 8, 90128 Palermo, Italy (corresponding author). E-mail: alessia.monaco@unipa.it

Note. This manuscript was submitted on March 3, 2016; approved on January 4, 2017; published online on March 17, 2017. Discussion period open until August 17, 2017; separate discussions must be submitted for individual papers. This paper is part of the *Journal of Structural Engineering*, © ASCE, ISSN 0733-9445.

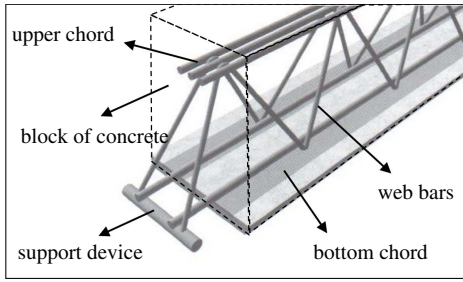


Fig. 1. Topology of HSTCB

This paper presents a numerical study of the failure behavior of HSTCBs. Of particular interest is the failure behavior of HSTCBs of different sizes. The influence of specimen size and geometry on structural failure has been observed and studied in structures made of many types of concrete materials, including normal-strength concrete (Bažant and Kazemi 1988; Ožbolt et al. 1994; Cedolin and Cusatis 2007, 2008; Syroka-Korol and Tejchman 2012), high-strength concrete (Appa Rao and Raghu Prasad 2004), and, more recently, basalt bar-reinforced concrete (Syroka-Korol and Tejchman 2013). Understanding of size and geometrical effects could lead to improved design procedure because many full-scale designs have to rely on the extrapolation of laboratory experiments on small-scale specimens. Meanwhile, analysis of size and geometrical effects has also stimulated the development of new cementitious composite materials with superior strength and toughness (Lepech and Li 2003, 2004) and has inspired advanced analysis

techniques for both classical and new problems (Bažant and Yu 2004; Yasir Alam and Loukili 2010; Yu et al. 2016).

This paper is planned as follows: the next section describes the procedure of the finite-element analysis, the third section presents model validation against both the existing experimental results and a more realistic computational model, the following section presents the simulated failure behaviors of HSTCBs of different sizes, and the fifth section discusses overall observed size and geometrical effects on the peak load capacity of HSTCBs.

Description of Finite-Element Analysis

The HSTCB is a complex three-dimensional structure composed of strain-softening concrete material and ductile steel reinforcement. The main challenge of developing a numerical model for a HSTCB is to determine which details should be retained and which neglected so that the model will be sufficiently robust and also computationally efficient for the design purpose. In the present FE model, the reinforcement bars and the bottom steel plate are modeled using beam and shell elements, respectively, and the concrete material is modeled using linear displacement tetrahedral elements. The mesh size is chosen through a convergence study of load-deflection curves.

Constitutive Models

In this study, the constitutive response of concrete is described by a continuum damage plasticity model (Lee and Fenves 1998), which combines the theory of continuum damage mechanics and the

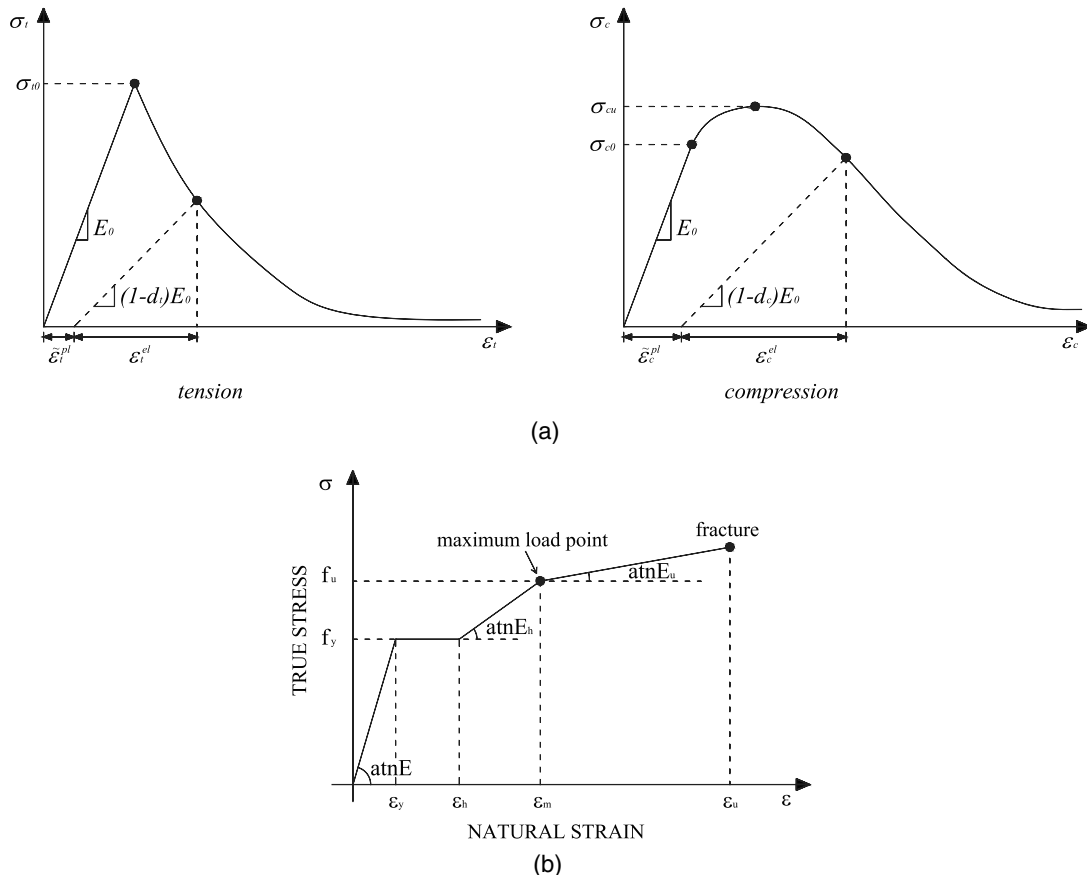


Fig. 2. Stress-strain curves of materials: (a) concrete under uniaxial tension and compression; (b) elastoplastic hardening behavior of steel

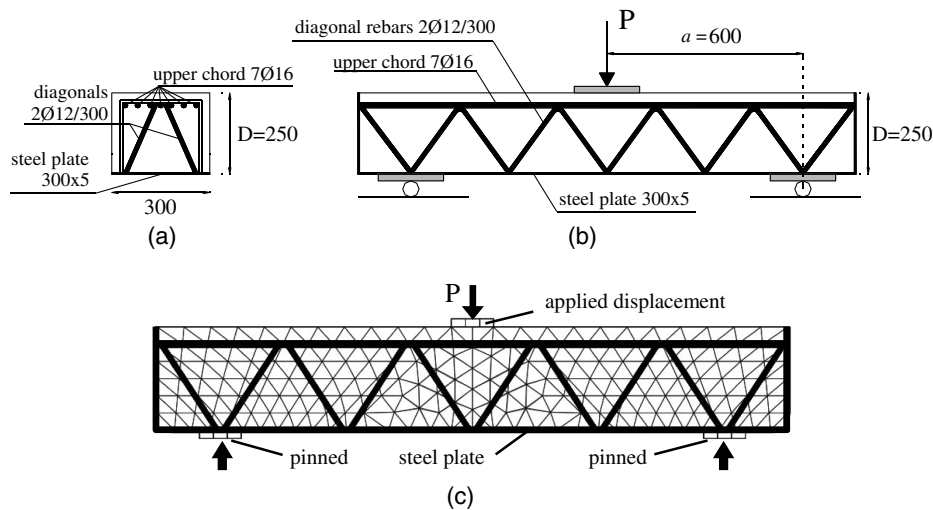


Fig. 3. Specimen S1 (dimensions in millimeters): (a) cross section; (b) longitudinal section and load condition; (c) mesh of elements and boundary conditions

theory of plasticity for a realistic representation of the inelastic behavior of concrete. Fig. 2(a) shows the stress-strain curves of concrete under uniaxial tension and compression. To mitigate the spurious mesh dependency of the FE simulation of concrete fracture due to its strain-softening behavior, the crack band model is used in the simulation (Bažant and Oh 1983). In the implementation, fracture energy G_f is used as an input parameter and, as a consequence, the tensile stress-strain curve is adjusted as a function of element size in order to preserve the constancy of the fracture energy. The constitutive relationship of steel material is considered to follow a metal plasticity model, which exhibits elastoplastic hardening behavior [Fig. 2(b)]. In this model, the von Mises yield surface with an isotropic hardening rule is used to describe the plastic flow, in which the yield surface changes its size uniformly in all plastic strain directions.

The interface between the steel bars and concrete material is assumed perfectly bonded. Such a simplification eliminates the need to model the highly nonlinear *stick-slip* type of behavior of the interface. As will be shown later, the validity of this assumption is assessed by comparing the predicted load-deflection curves with experimental measurements as well as those calculated by a model in which the interface is modeled by using a set of nonlinear cohesive elements.

Geometrical Scaling of Specimens

To investigate the influence of size and geometry on the failure behavior of HSTCBs, the authors performed numerical simulations of three-point bending tests on HSTCBs of three sizes, henceforth referred to as Specimens S1, S2, and S3. The simulations were performed using the general-purpose FE analysis software *ABAQUS 6.12*. Figs. 3(a and b) show the details of the geometry, boundary conditions, and steel reinforcement of the beam examined in Specimen S1. In the scaled Specimens S2 and S3, the span-to-depth ratio is kept the same as that of Specimen S1 (i.e., $a/D = 2.4$), and the depths are chosen so that Specimens S1, S2, and S3 have size ratio 1:2.22:4.93. The width of the beam is chosen as a constant ($b = 300$ mm). The size of the steel bars and bottom steel plates is kept constant according to current industrial practice, whereas the horizontal span of the diagonal steel truss is linearly scaled with beam depth. Fig. 4 shows the scaled models with their geometrical

dimensions. It is noted that Specimens S1 and S2 represent the typical sizes that are used in practice.

It is clear that the resulting cross sections of the three specimens differ from each other in terms of the slope of the diagonal rebars, which increases from 68° for Specimen S1 to 86° for Specimen S3. Furthermore, the sizes of the bottom steel plate and diagonal rebars are also not scaled with beam size. Therefore, the present three specimens do not exhibit geometrical similarity. As will be discussed later, this has a profound implication on the failure behavior of the beams. All specimens are considered made of the same type of material, i.e., concrete with compressive strength 25 MPa, Class B450C steel for the longitudinal and diagonal rebars, and Class S355 steel for the bottom plate.

Model Validation

The proposed computational model was used to simulate a recent three-point bending experiment on Specimen S1 (Monaco 2014, 2016; Colajanni et al. 2016a). The simulation result is compared with the experimental observation as well as a FE benchmark simulation, in which a more realistic cohesive law for the steel-concrete interface was used. These comparisons allow justification of the simplified assumption of perfect bonding in the steel-concrete interface for the purpose of predicting the load capacity of HSTCBs.

Comparison with Experimental Results

Several three-point bending tests were performed on Specimen S1 at the Laboratory of Structures of the University of Palermo (Monaco 2014, 2016; Colajanni et al. 2016a). As shown in Fig. 3, the cross section of the specimen has a dimension of 250 mm depth and 300 mm width, and the basic steel truss consists of seven 16-mm-diameter rebars on the top, a 5-mm-thick steel plate at the bottom, and a couple of 12-mm-diameter rebars along the diagonal directions.

The rebars are made of Class B450C ribbed steel, which has yielding strength $f_y = 450$ MPa, and the bottom plate is made of Class 355 smooth steel with $f_y = 355$ MPa. For concrete, the design compressive strength, f_c , is equal to 25 MPa. The specimens have a shear span equal to 600 mm and the bottom steel plate is anchored at the ends of the beam in order to avoid slip between the plate and the concrete.

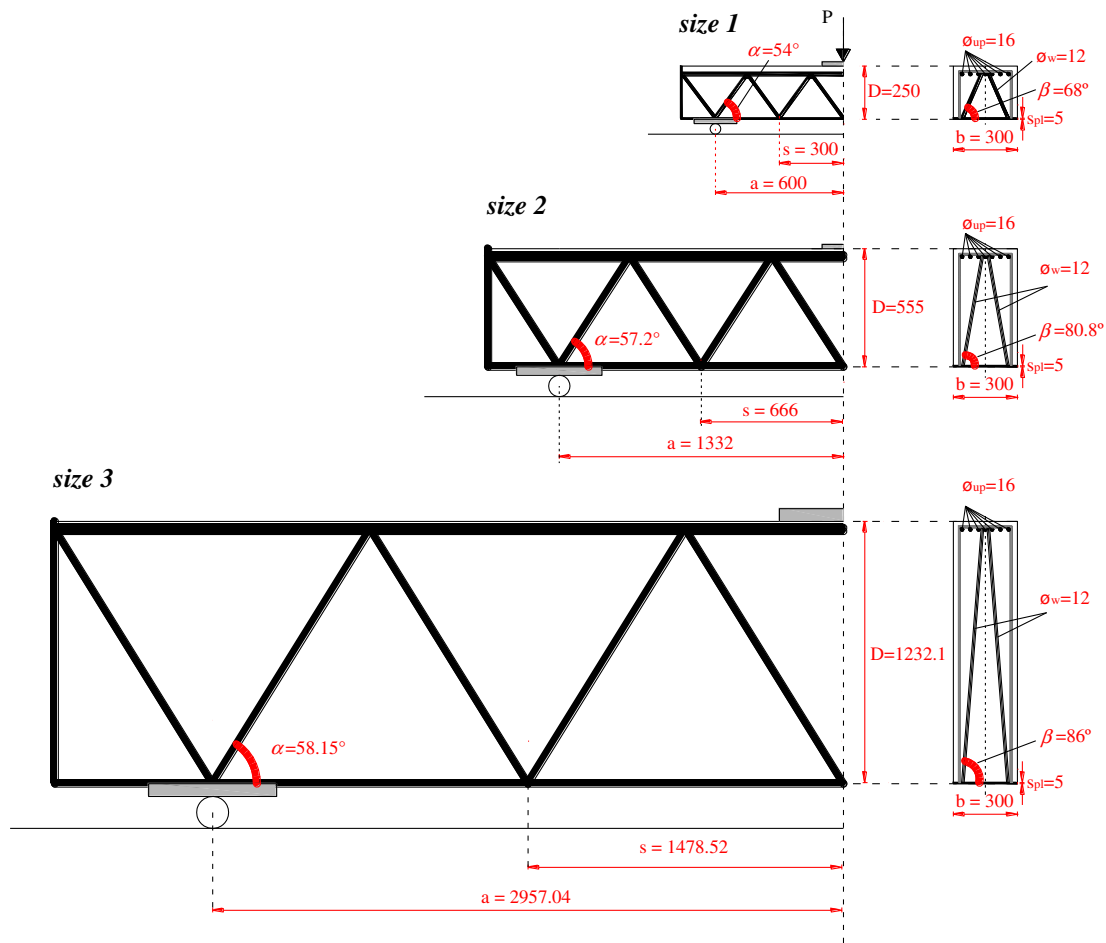


Fig. 4. FEM model features (dimensions in millimeters): symbols of geometric parameters and ratio between geometry of models

Two replicates of Specimen S1, denoted A1-1 and A1-2 in this paper, were tested in the laboratory. These tests were performed by using a displacement-controlled load, i.e., the load was applied through a hydraulic jack, which was able to produce a constant displacement increment. During the test, the midspan displacement was monitored by external LVDTs, and the strains in the steel bars and the bottom plates were measured by strain gauges. With reference to the experimental load-deflection curves of both the A2-1 and A2-2 specimens (Fig. 5), flexural cracks started to develop at the bottom of the specimens as the load reached about 120 kN. Upon continued loading, diagonal shear cracks started to initiate and propagate, whereas the growth of the aforementioned flexural cracks became insignificant. When the beam reached its peak strength, significant diagonal shear cracking was observed, which led to the subsequent loss of load capacity. Finally, the embedded ductile steel trusses allowed the beam to retain a residual load capacity of about 200 kN at a large displacement greater than 25 mm (Colajanni et al. 2016a).

The authors used the present FEM model to simulate the aforementioned experiments. Fig. 5 presents the comparison between the simulated and measured load-displacement curves. It is evident that the present model overestimates the stiffness of the beam due to the assumed perfect bonding condition of the steel-concrete interface. As will be shown in the following section, the simulated elastic response can be further improved by employing a more realistic nonlinear model for the concrete-steel interface. The simulation results show that the beam exhibits an overall brittle failure, which is manifested by a sudden drop in load-carrying capacity right after

the peak load. After this drop, the beam exhibits a residual load-carrying capacity.

At the initial stage of loading, the concrete experienced flexural damage at the bottom of the beam followed by yielding of the steel truss and plate. The flexural failure of concrete did not lead to a significant loss of load capacity because the tensile stress generated by the bending was taken primarily by the steel elements (i.e., the bottom plate in HSTCBs). Therefore, the flexural damage (flexural cracks) experienced by the tensile concrete at the first stage did not contribute to the failure of the beam. As the beam attained its peak strength, extensive compressive failure occurred almost along the direction of the compressed diagonal steel bars in the form of a narrow band. This indicates that a compression strut was formed along the diagonal direction, which started to experience damage signifying diagonal shear failure. However, it should be also noted that the span-to-depth ratio that characterizes the geometry of Specimen S1 did not allow the typical truss mechanism, which is sometimes used to interpret the shear failure of conventional RC beams, to be triggered. After the load-deflection curve entered its post-peak regime, the damage in the compression strut continued to grow and eventually led to the ultimate failure of the beam. The experimental results indicate that Specimen A2-1 reached a peak load of 422.29 kN at a midspan deflection of 6 mm, whereas Specimen A2-2 exhibited a maximum load of 461.29 kN at a midspan displacement of 8 mm. Thus, Specimen A2-2 exhibited a peak load 9.23% higher than Specimen A2-1, which is within the normal scattering range of experimental results on RC specimens (Bažant 2005; Yu et al. 2016). With reference to the postpeak

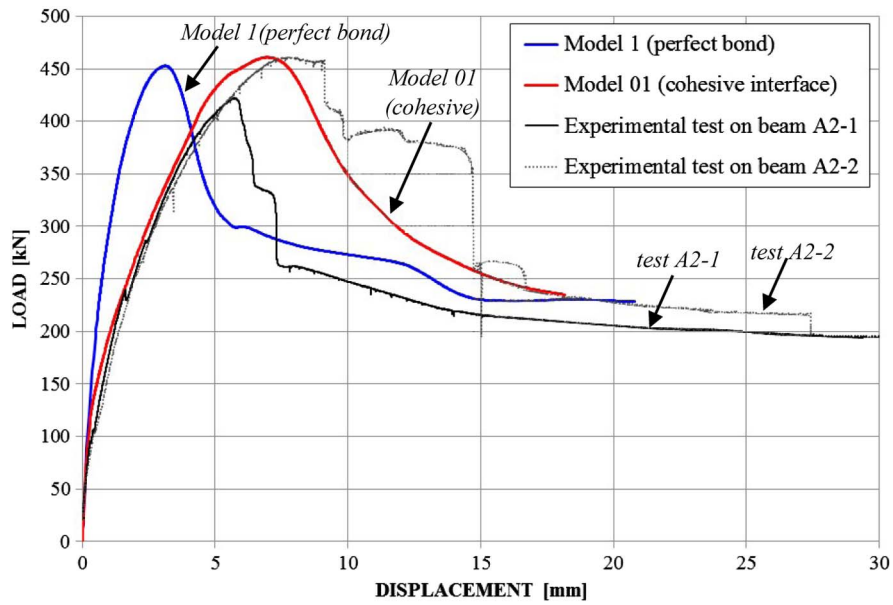
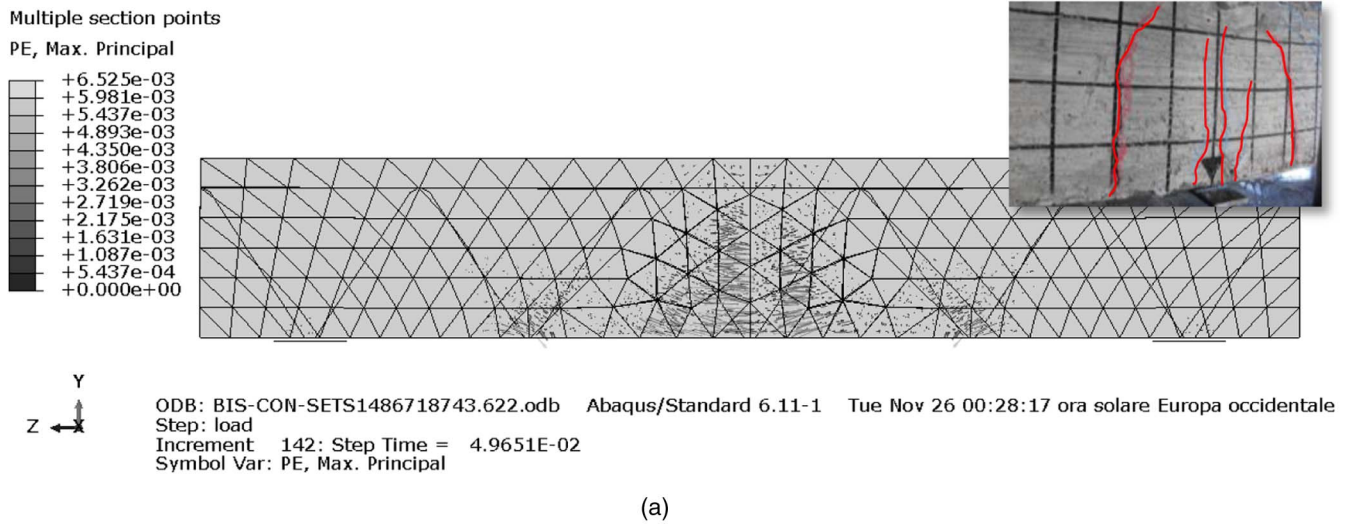
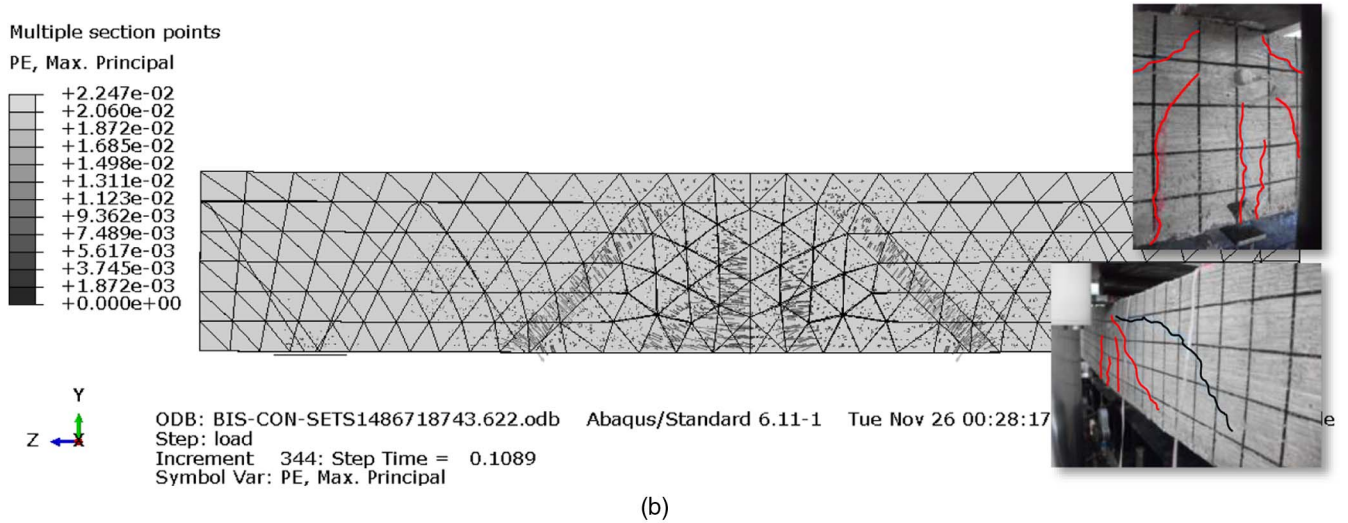


Fig. 5. Comparison between detailed and simplified FEM models against experimental results for HSTCBs with added longitudinal reinforcement



(a)



(b)

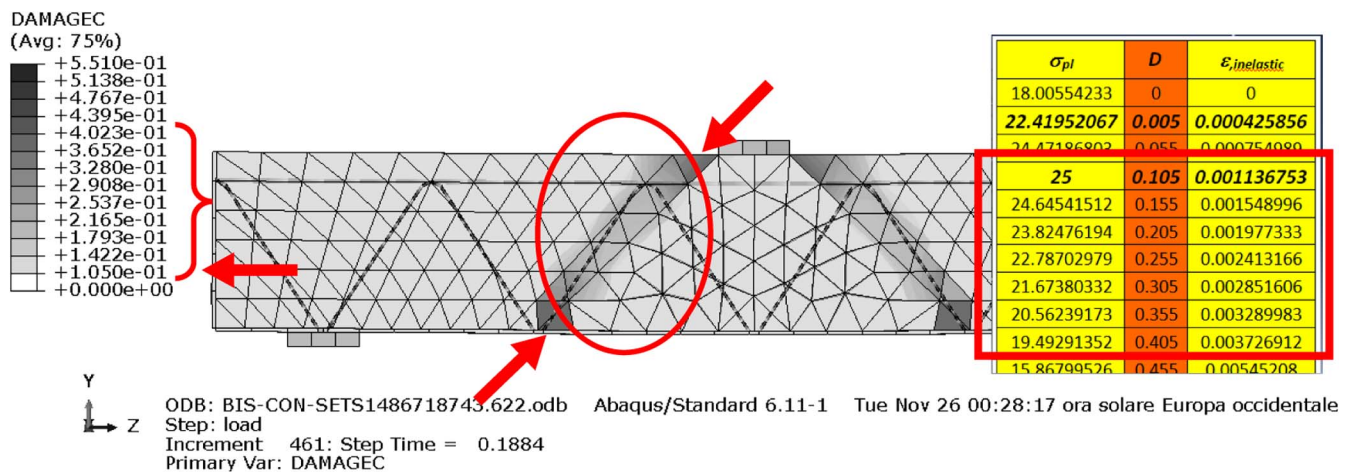
Fig. 6. Simulated maximum principal strains and comparisons with observed fracture patterns in Specimen S1: (a) subvertical cracks at initial loading stage; (b) growth of cracks in midspan and along diagonal direction right before peak load

trend of the experimental curves, it is noted that both specimens exhibited a subhorizontal branch with values of residual load capacity comparable in the two cases (about 200 kN): the residual load capacity at large displacement values is attributed to the steel elements that were seen to provide a ductile response in the final phases of the test. The measurements of the strain gauge showed that for both specimens the bottom tensile plate yielded shortly after peak load was reached. The attainment of peak load and the subsequent sudden load drop can be attributed to the extensive failure of the concrete strut before the ductility of the diagonal steel bars was mobilized to contribute to the overall structural behavior. The strain gauge measurements showed that the longitudinal rebar of the upper chord remained elastic until the end of the test.

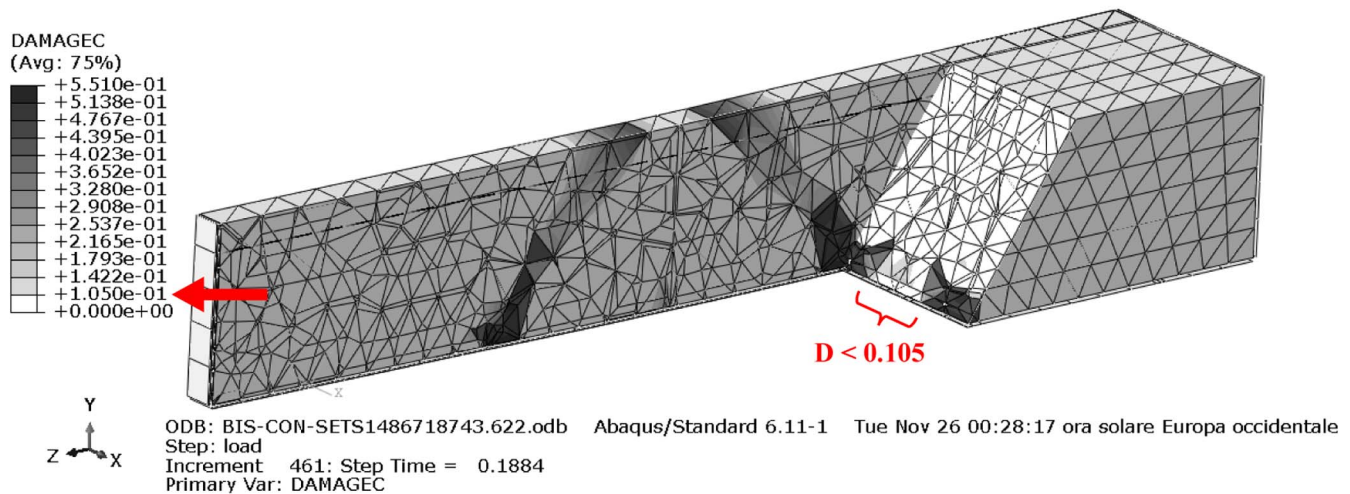
Overall, the failure of these two beams can be described by the following stages: (1) development of subvertical flexural cracks in the midspan before the achievement of peak load; (2) diagonal shear cracking involving the development of cracks along the steel diagonals, in the direction of the compressed concrete strut as peak load is reached; (3) propagation of the diagonal cracks along the steel diagonals, with insignificant growth of the flexural cracks, and crushing of the concrete strut, which causes the sudden drop of load-carrying capacity; and (4) development of residual capacity due to ductile behavior of the steel members.

Fig. 6(a) shows the simulated profile of the maximum principal strain in the beam during the initial loading stage. It can be seen that the flexural subvertical cracks first appear in the midspan of the beam and two symmetrical diagonal cracks begin to develop. Fig. 6(b) shows the direction of the maximum principal strain right before the beam reaches its peak strength. Compared to Fig. 6(a), it is evident that the flexural cracks do not exhibit substantial growth, whereas the compressive damage along the two diagonal directions grows significantly. These simulated damage patterns agree well with the experimentally observed cracking pattern, as shown in the insets of Figs. 6(a and b).

The present constitutive model of concrete uses damage parameter α_c ranging from 0 to 1 to describe the extent of compressive damage ($\alpha_c = 0$ denotes the intact condition, and $\alpha_c = 1$ denotes complete damage). This damage parameter can be understood as a parameter describing the loss of the unloading elastic stiffness of the material [Fig. 2(a)]. The damage index used in this study describes the compressive damage extent of concrete, for which the stress-strain curve can be described as $\sigma_c = (1 - \alpha_c)E_0(\varepsilon_c - \tilde{\varepsilon}_c^{pl})$, in which σ_c and ε_c represent the concrete stress and strain, respectively; E_0 = elastic stiffness; and $\tilde{\varepsilon}_c^{pl}$ = plastic strain [Fig. 2(a)]. If the plastic strain is ignored, the damage index essentially measures the degradation of the secant stiffness. Fig. 7 shows the profile of the compressive damage parameter in the beam at peak load.



(a)

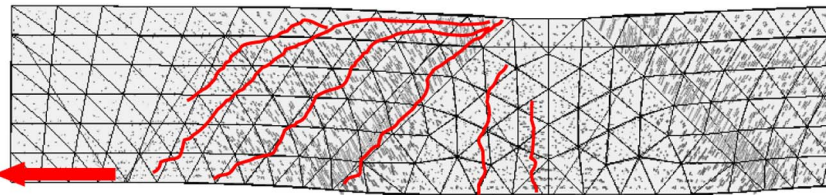
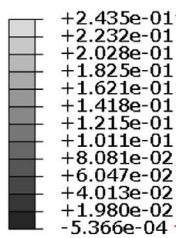


(b)

Fig. 7. Magnitude of damage variable at failure in S1: (a) frontal view of concrete strut; (b) axonometric view

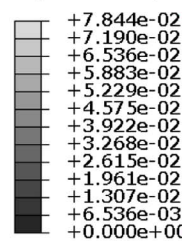
Multiple section points

PE, Max. Principal



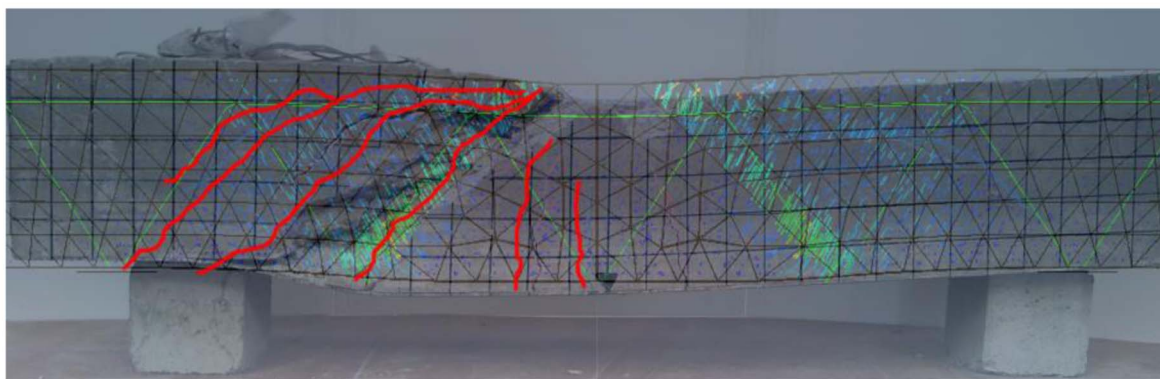
Multiple section points

PE, Max. Principal



ODB: BIS-CON-SETS1486718743.622.odb Abaqus/Standard 6.11-1 Tue Nov 26 00:28
 Step: load
 Increment: 1303: Step Time = 0.8509
 Symbol Var: PE, Max. Principal

(a)



(b)

Fig. 8. Crack pattern at end of analysis in S1 and comparison with experimental evidence: (a) frontal view of numerical cracks; (b) picture of Specimen A1-2 at end of test compared to numerical cracks

It is seen that at peak load the maximum value of α_c along the diagonal direction is about 0.105. According to the stress-strain curve of concrete, this damage level indicates that the material element is about to reach its compressive strength. By cutting the cross section along the compression strut, it is observed that the maximum compressive damage occurs near the surfaces of the beam at the bottom of the compression strut, which corresponds to the location where the diagonal steel truss is attached to the bottom steel plate. Such a concentrated damage pattern could be attributed to the stress concentration at the interface produced by the mismatch of the elastic properties of concrete and steel.

Fig. 8 shows the cracking pattern of the beam at the end of the analysis. It is seen that one major diagonal crack propagates throughout the beam depth accompanied by several small diagonal cracks. Simulation shows that the maximum value of α_c along the diagonal compression strut reaches 0.855, indicating an extensive amount of compressive damage. Meanwhile, the stresses in the steel truss and plates are well beyond the material's yield strength but do not yet reach the material's rupture strength. As shown in Fig. 8, the simulated diagonal cracking pattern at the ultimate failure point agrees well with the experimental observation.

The aforementioned comparison indicates that, despite the use of a simple interfacial model, the present model can accurately capture various essential failure mechanisms, as well as the peak load capacity of the beam, even though it does not accurately predict the initial elastic stiffness of the beam.

Comparison with Computational Benchmark

To further investigate the role of steel-concrete interfacial behavior, the authors simulated the three-point bending test of Specimen S1 by considering a nonlinear model for the steel-concrete interface. The resultant interfacial slip was determined as $\delta = \sqrt{\delta_s^2 + \delta_t^2}$, where δ_s and δ_t are the slips along the two orthogonal directions in the plane of the interface. The work-conjugate effective shear traction needs to satisfy

$$\tau d\delta = t_s d\delta_s + t_t d\delta_t \quad (1)$$

where t_s and t_t are shear tractions in two orthogonal directions in the interface plane. Eq. (1) has to be satisfied for any arbitrary values of $d\delta_s$ and $d\delta_t$. This condition yields $t_s = \tau\delta_s/\delta$ and $t_t = \tau\delta_t/\delta$. Therefore, the behavior of the steel-concrete interface can be described by the relationship between the net slip and the effective shear traction. In this model, the τ - δ relationship is considered to follow the well-known bond-slip model developed by Eligehausen et al. (1983) as shown in Fig. 9. For the numerical implementation of this model, the rising branch of the curve was linearized in such a way that the total energy dissipation (i.e., the area under the τ - δ curve) is preserved (Fig. 9).

Fig. 5 shows the load-deflection curve simulated by this detailed FEM model together with that simulated by the proposed simplified model and the experimental measurement. It is seen that the result of the benchmark model agrees well with the experimental result. As compared to the simulation using the simplified model, it is

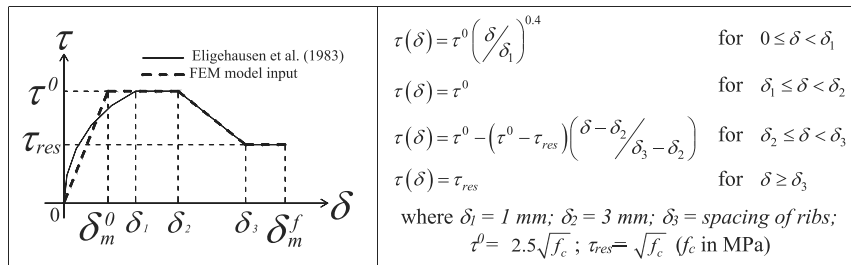


Fig. 9. Cohesive law based on bond-slip relationship (data from Eligehausen et al. 1983)

clear that employing a realistic steel-concrete interface allows better capture of the overall beam stiffness. However, it is interesting to note that it does not significantly affect peak load or total energy dissipation (i.e., the area under the load-displacement curve). This implies that the steel-concrete interface does not experience significant damage. In other words, the energy dissipation along this interface is small compared to the dissipation due to concrete damage and steel plasticity. Therefore, the present simplified model is sufficient for modeling the failure behavior of Specimen S1. It should also be pointed out that, compared to those of the benchmark model, the computations of the present model can be performed more than three times faster.

Numerical Simulations of Specimens S2 and S3

The authors used the present model to simulate the failure behavior of Specimens S2 and S3. As discussed in the previous section, the perfect-bond model yielded a reasonable prediction of the failure mechanisms of Specimen S1 because the damage of the steel-concrete interface had an insignificant effect on the overall failure behavior of the beam. Similar to the process for Specimen S1, the authors also used the benchmark model to simulate the behavior of Specimens S2 and S3 to compare with the present model. Fig. 10 shows the simulated load-deflection curves of Specimens S2 and S3 by using the present model and the benchmark model. It is seen that the load-deflection curves simulated by these two models are very similar. It is interesting to observe that for Specimens S2 and S3 the difference in the initial rising portions of the load-deflection curves simulated by the two models is less pronounced than that for Specimen S1. This could be due to the fact that the initial elastic response of the steel-concrete interface has less influence on the elastic response of Specimens S2 and S3 because the dimension of the steel truss is not scaled proportionally with the concrete beam size. The difference in the post-peak regime predicted by these two models will be explained in the next two sections based on the failure behavior of these specimens.

Load-Deflection Curve and Failure Behavior of Specimen S2

Fig. 10 indicates that, in contrast to Specimen S1, Specimen S2 exhibits fairly ductile behavior before the ultimate loss of its load capacity. During the initial stage of loading, it was observed that concrete damage occurred in the midspan of the beam. It was noted that, under loading, the bottom steel plate was pulled upward by the two diagonal truss bars, which introduced local compressive stress on the concrete [Fig. 11(a)]. When the specimen achieved peak load, the bottom plate and the diagonal rebars of the truss had already yielded and a significant number of flexural cracks were present in the concrete. In the diagonal direction, the stress in the concrete reached the compressive strength. Meanwhile, limited

compressive failure was also observed in the midspan of the beam due to the local deformation of the bottom plate.

It is noted that the overall damage along the diagonal directions was much less than the flexural damage in the midspan of the beam [Fig. 11(b)]. This is very different from the failure mechanism of Specimen S1, in which the majority of cracking was observed along the diagonal directions. Because the compressive damage along the diagonal directions in Specimen S2 was less significant, the beam was able to exhibit an overall ductile behavior. The delay in compressive failure in the diagonal directions in Specimen S2 may be attributed to the fact that in the transverse direction the steel truss has a steeper angle (Fig. 4), which leads to more confinement of the concrete material, and such confinement effectively suppresses diagonal shear cracking. Certainly, other factors, such as the aspect ratio of the cross section, may also influence the failure

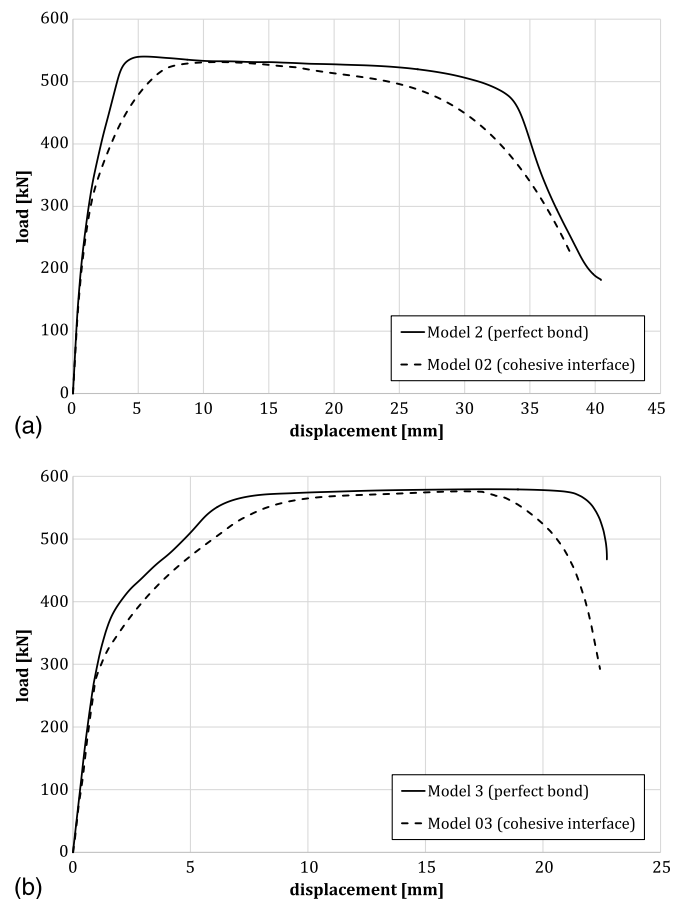


Fig. 10. Simulated load-displacement curves for (a) Specimen S2; (b) Specimen S3

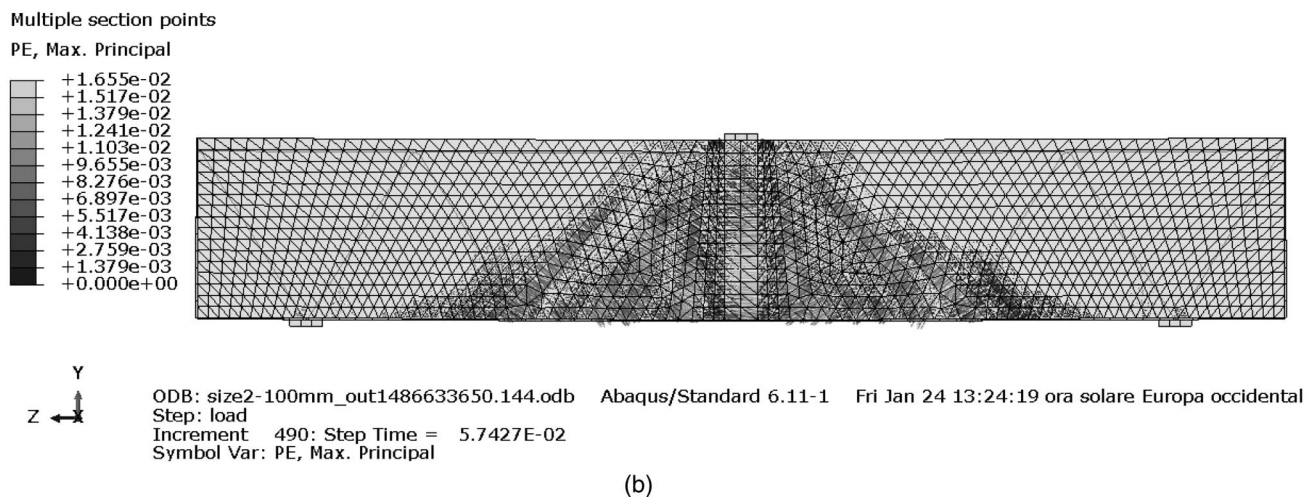
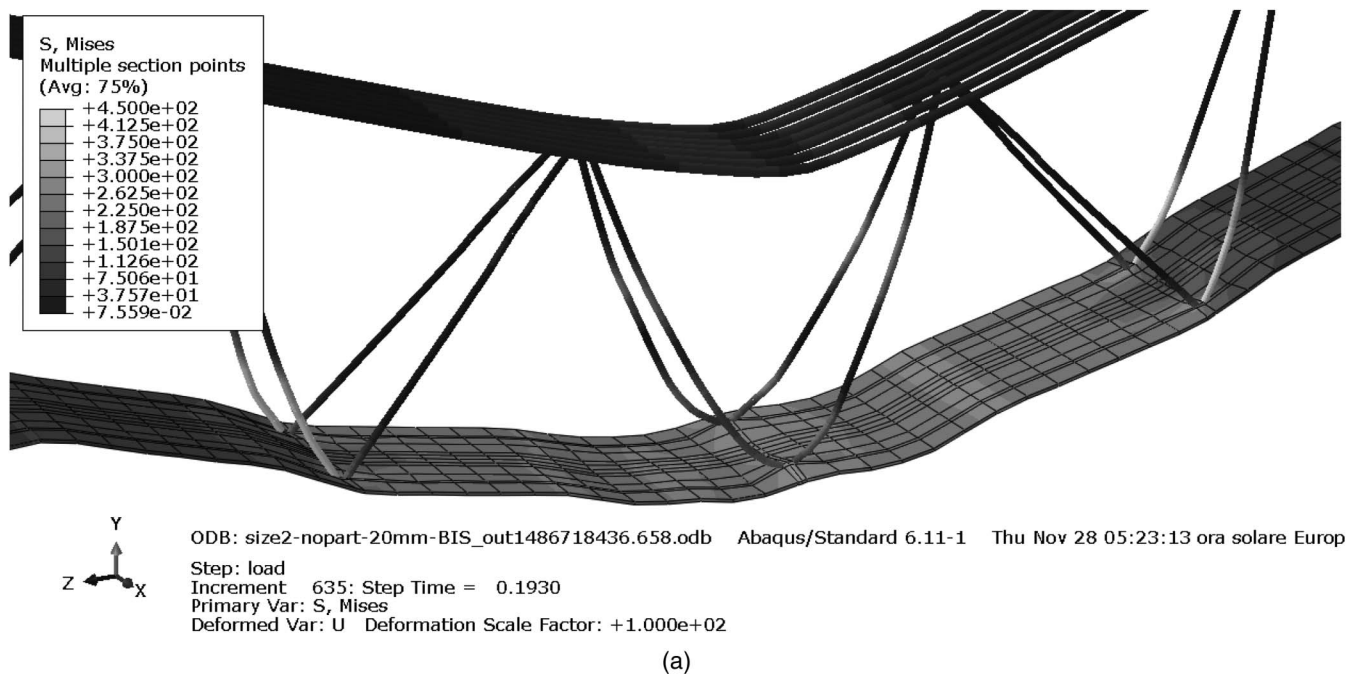


Fig. 11. Damage mechanism of Specimen S2: (a) local deformation of steel truss; (b) maximum strain profile showing dominant flexural cracking

behavior of the beam. A detailed parametric study will be needed to elucidate these influences.

Because the dominant failure mode of Specimen S2 was not diagonal shear failure, it was expected that the interfacial damage between the concrete material and diagonal rebars of Specimen S2 would be less than that of Specimen S1. Therefore, as seen in Fig. 10, the postpeak regime of the load-deflection curve simulated by the present model is close to that simulated by the benchmark model.

Load-Deflection Curve and Failure Behavior of Specimen S3

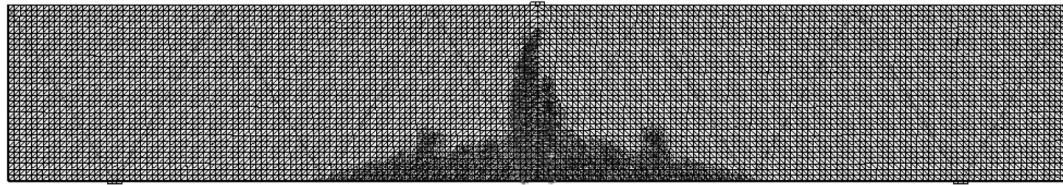
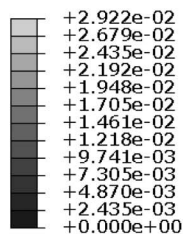
For Specimen S3, a set of diffuse cracks appeared at the bottom of the beam during the initial loading stage. These flexural cracks were followed by compressive damage along the diagonal direction [Fig. 12(a)]. At peak load, the main failure mechanism can be described as flexural damage at the midspan [Fig. 12(b)]. After peak load was attained, the maximum plastic principal strains in the diagonal directions continuously increased. It is worthwhile to note

that the width of the cracks in the diagonal direction tended to increase at the bottom of the beam, which is comparable to the flexural crack pattern [Fig. 12(c)]. Such a cracking pattern remained almost the same until the ultimate failure of the beam.

By comparing the failure behaviors of Specimens S2 and S3, it is clear that Specimen S3 exhibited less ductility. Even though the steel truss bars in S3 had a steeper angle in the transverse direction, it was noted that along the span direction the volume of concrete material between the steel trusses in Specimen S3 was larger than in Specimen S2. Therefore, the confinement effect on the compressive damage along the diagonal directions was less significant in Specimen S3 compared to that in Specimen S2. Meanwhile, as compared to S1, the failure behavior of Specimen S3 was more ductile, which indicates that the confinement effect in Specimen S3 was more pronounced. The combined flexural and shear damage in the postpeak regime also explains the observation that the difference in the postpeak regimes of the load-deflection curves simulated by the present model and the benchmark model became more pronounced compared to that of Specimen S2, in which only flexural damage was dominant in the postpeak regime.

Multiple section points

PE, Max. Principal

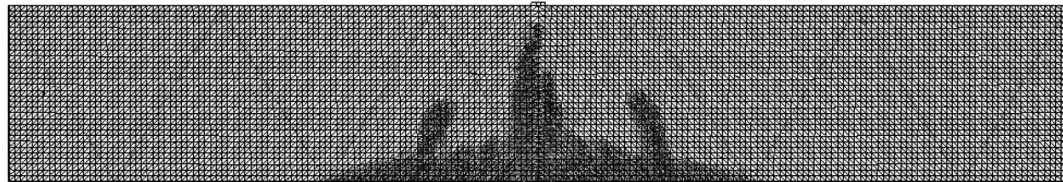
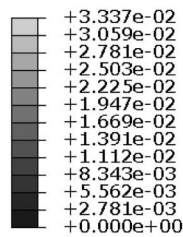


ODB: size3-nopartiz1486552814.399.odb Abaqus/Standard 6.11-1 Tue Nov 05 18:55:55 ora solare Europa occidentale 2
 Step: load
 Increment 450: Step Time = 0.1346
 Symbol Var: PE, Max. Principal

(a)

Multiple section points

PE, Max. Principal

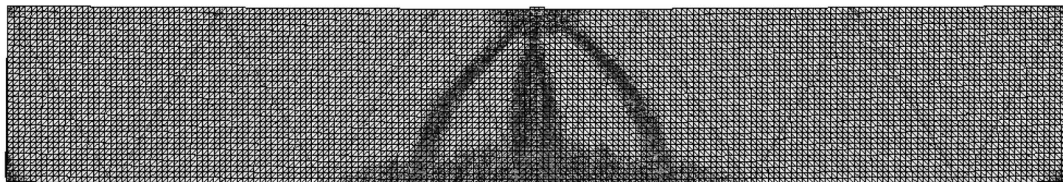
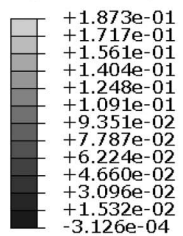


ODB: size3-nopartiz1486552814.399.odb Abaqus/Standard 6.11-1 Tue Nov 05 18:55:55 ora solare Europa occidentale 2
 Step: load
 Increment 620: Step Time = 0.1552
 Symbol Var: PE, Max. Principal

(b)

Multiple section points

PE, Max. Principal



ODB: size3-nopartiz1486552814.399.odb Abaqus/Standard 6.11-1 Tue Nov 05 18:55:55 ora solare Europa occidentale 2
 Step: load
 Increment 1560: Step Time = 0.9982
 Symbol Var: PE, Max. Principal

(c)

Fig. 12. Evolution of cracking patterns of Specimen S3: (a) at initial loading stage; (b) at peak load; (c) at ultimate failure

Discussion on Scale and Geometrical Effects in Failure of HSTCB

The foregoing simulations revealed that the failure behavior of HSTCBs strongly depends on their size and geometry. Based on the present simulations, there are two main failure modes in concrete:

(1) flexural failure at the midspan, and (2) diagonal shear failure. The flexural failure of HSTCBs can essentially be described as a ductile mode because the load is primarily resisted by the bottom steel plate after the concrete material is cracked in tension. In contrast, diagonal shear failure is typically quasi-brittle in nature, which is manifested by a gradual loss of load-carrying capacity after peak load is attained.

It is observed that the relative dominance of these two failure modes is strongly influenced by the 3D geometrical arrangement of the steel truss, which potentially leads to different levels of confinement effect on the concrete material. For reinforced concrete beams, the size effect on load capacity can be studied analytically for geometrically similar specimens, provided they have the same failure mode. However, the three HSTCB specimens considered in the present study do not follow geometrical similarity and, therefore, existing analytical scaling models (e.g., Bažant 1984, 2000, 2005) are not applicable. Nevertheless, the simulated size and geometrical effects on the peak load of HSTCBs can be explained qualitatively.

For size effect analysis, it is customary to use nominal structural strength, σ_N , which is defined as a load parameter of a dimension of stress, i.e.

$$\sigma_N = P_{\max}/bD \quad (2)$$

where P_{\max} = maximum load capacity of beam; D = characteristic size of beam (beam depth in present analysis); and b = beam width.

For Specimen S1, the failure mode at peak load was characterized by diagonal shear failure. The size effect on the nominal strength of RC beams for such a global failure mode has been investigated extensively, and an approximate size and geometrical effect equation has been proposed (Bažant 1984, 2005)

$$\sigma_N = \sigma_0(1 + D/D_0)^{-1/2} \quad (3)$$

where σ_0 = nominal structural strength at small-size limit; and D_0 = transitional size. Both σ_0 and D_0 are dependent on structural geometry, material strength, and fracture properties. It is noted that Eq. (3) describes the transition from quasi-plastic shear failure to brittle shear failure as the specimen size becomes much larger than the size of the fracture process zone.

It should be noted that Eq. (3) was proposed to describe the general size effect in a quasi-brittle fracture, in which a large preexisting (fatigued) crack is formed prior to peak load. Recent studies have demonstrated that Eq. (3) can accurately describe the observed size effect on the diagonal shear failure of RC beams that exhibit diagonal shear cracks (Bažant and Yu 2005; Yu et al. 2016). The shear failure of HSTCBs observed in this study [Fig. 6(b)] essentially has the same mechanism as the diagonal shear failure of conventional RC beams. Therefore, Eq. (3) is expected to provide a sufficient approximation of the size effect in shear failure of HSTCBs.

As peak load was attained in Specimens S2 and S3, both specimens experienced a significant level of flexural damage at the mid-span and much less damage along the diagonal directions. If concrete damage is ignored in the diagonal directions and the tensile stress in the bottom part of the beam is considered taken by the yielded steel plate, then the bending moment capacity at the mid-span can be calculated as $M_u = F_y A_s \bar{d}$ (F_y = steel yield strength; A_s = cross-sectional area of steel plate; and \bar{d} = effective depth of beam, i.e., distance between centroid of steel plate and centroid of compressive stress block of the concrete). Therefore, the peak load of the beam under three-point bending can be calculated as $P_u = 4F_y A_s \bar{d}/L$. Because the dimension of the beam is geometrically scaled in two dimensions, \bar{d}/L can approximately be taken as a constant. This indicates that load capacity is independent of beam size, and the corresponding scaling equation for σ_N can be written as

$$\sigma_N = \eta D^{-1} \quad (4)$$

where $\eta = 4F_y A_s \bar{d}/bL$.

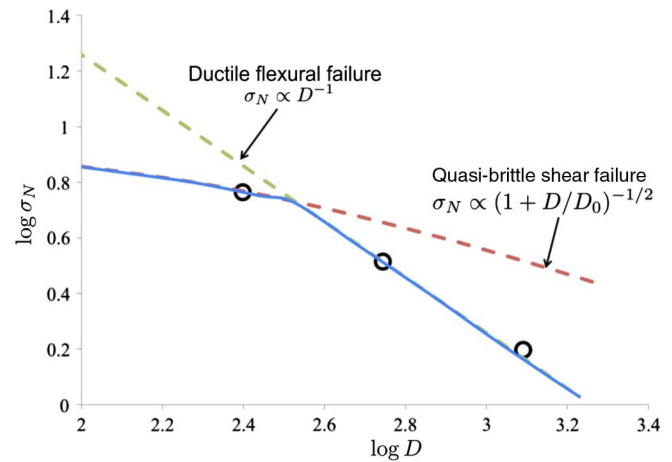


Fig. 13. Simulated size effect on nominal structural strength

Fig. 13 plots the simulated relationship between the nominal strengths of Specimens S1–S3 and their sizes on the log-log scale, together with Eqs. (3) and (4). Because there is only one simulation point for the diagonal shear failure mode, it is not possible to determine σ_0 and D_0 of Eq. (3) and, therefore, for the purpose of illustration, only a schematic plot of Eq. (3) is shown in Fig. 13. Nevertheless, this is sufficient to explain the behavior of the size effect curve. It is clear that, for Specimens S2 and S3, the simulated size effect is consistent with Eq. (4). For Specimen S1, the simulated nominal strength is expected to follow Eq. (3).

Based on the aforementioned analysis, the nominal strength of the beam can be understood as the minimum value of the nominal strengths predicted by Eqs. (3) and (4), i.e.

$$\sigma_N = \min[\eta D^{-1}, \sigma_0(1 + D/D_0)^{-1/2}] \quad (5)$$

It is noted that there is a transition between these two size effects, which is governed by both the size and geometry of the beam. Due to the complicated geometry of the embedded steel truss and its confinement effect on the concrete material, it is not feasible to obtain a simple analytical solution for the nominal strength of HSTCB that takes into account both failure modes. Therefore, a robust and efficient computational model is essential.

It is interesting to see that Eq. (5) predicts size effect $\sigma_N \propto D^{-1}$ for the flexural failure mode. This is due to the fact that in the present analysis the bottom steel plate is not scaled proportionally with the beam size because current industrial practice typically uses a 5-mm-thick plate. This greatly penalizes the nominal strength for large-size beams. If the steel plate thickness were proportionally scaled with the beam size, the size effect on nominal strength for the flexural failure mode would vanish. As a result, only the diagonal shear failure mode, which could be subjected to a strong size effect in the absence of shear stirrups, would be observed (Bažant and Yu 2005; Yu et al. 2016). It should be noted that this size effect in diagonal shear failure would also be influenced by the complex geometry of the steel truss of HSTCBs, which has to be studied through 3D computational modeling.

Conclusions

A robust and efficient FE model was developed to study the failure behavior of HSTCBs. Through both experimental and numerical validations, it was found that detailed modeling of the steel-concrete interface is not essential for predicting the peak load

capacity or overall energy dissipation of the beam. Simulations of HSTCBs of different sizes under three-point bending showed two distinct failure mechanisms, namely, flexural failure at the midspan and diagonal shear failure. The resulting size and geometrical effects on peak load capacity can be described as a combination of the two individual size effects of these failure modes, in which the size effect in diagonal shear failure can be described by the classical Bažant's size effect law of quasi-brittle fracture and the size effect in ductile flexural failure can be derived by using a simple plastic analysis. The transition between these two size effects is influenced by the 3D geometry of the HSTCB and the fracture property of concrete. Because analytical modeling of this complete size effect is not feasible, robust and efficient computational modeling becomes an indispensable tool for design extrapolation of HSTCBs across different sizes and geometries.

References

- ABAQUS [Computer software]. Dassault Systèmes Simulia, Providence, RI.
- Amadio, C., Macorini, L., Sorgon, S., and Suraci, S. (2011). "A novel hybrid system with RC-encased steel joists." *EJECE*, 15(10), 1433–1463.
- Appa Rao, G., and Raghu Prasad, B. K. (2004). "Size effect in structural high strength concrete." *Proc., 5th Int. Conf. on Fracture Mechanics of Concrete and Concrete Structures (FraMCOS-5)*, Vail, CO, 1083–1089.
- Badalamenti, V., La Mendola, L., and Colajanni, P. (2010). "Seismic behavior of hybrid steel trussed concrete beams." *Proc., 14th European Conf. Earthquake Engineering*, Curran Associates, Red Hook, NY, 1–8.
- Bažant, Z. P. (1984). "Size effect in blunt fracture: Concrete, rock, metal." *J. Eng. Mech.*, 10.1061/(ASCE)0733-9399(1984)110:4(518), 518–535.
- Bažant, Z. P. (2000). "Size effect." *Int. J. Solids. Struct.*, 37(1–2), 69–80.
- Bažant, Z. P. (2005). *Scaling of structural strength*, 2nd Ed., Hermes-Penton Science, London.
- Bažant, Z. P., and Kazemi, M. T. (1988). "Brittleness and size effect in concrete structures." *Proc., Engineering Foundation Conf. on Advances in Cement Manufacture and Use*, Engineering Foundation, New York.
- Bažant, Z. P., and Oh, B.-H. (1983). "Crack band theory for fracture of concrete." *Mater. Struct.*, 16(3), 155–177.
- Bažant, Z. P., and Yu, Q. (2004). "Size effect in concrete specimens and structures: New problems and progress." *Proc., 5th Int. Conf. on Fracture Mechanics of Concrete and Concrete Structures (FraMCOS-5)*, Univ. of Michigan, Ann Arbor, MI, 153–162.
- Bažant, Z. P., and Yu, Q. (2005). "Designing against size effect on shear strength of reinforced concrete beams without stirrups: I. Formulation." *J. Struct. Eng.*, 10.1061/(ASCE)0733-9445(2005)131:12(1877), 1877–1885.
- Campione, G., Colajanni, P., and Monaco, A. (2016). "Analytical evaluation of steel-concrete composite trussed beam shear capacity." *Mater. Struct.*, 49(8), 3159–3176.
- Cedolin, L., and Cusatis, G. (2007). "Cohesive fracture and size effect in concrete." *Proc., 6th Int. Conf. on Fracture Mechanics of Concrete and Concrete Structures (FraMCOS-6)*, Taylor & Francis, Abingdon, U.K., 18–21.
- Cedolin, L., and Cusatis, G. (2008). "Identification of concrete fracture parameters through size effect experiments." *Cem. Concr. Compos.*, 30(9), 788–797.
- Chisari, C., and Amadio, C. (2014). "An experimental, numerical and analytical study of hybrid RC-encased steel joist beams subjected to shear." *Eng. Struct.*, 61, 84–98.
- Colajanni, P., La Mendola, L., Latour, M., Monaco, A., and Rizzano, G. (2015a). "FEM analysis of push-out test response of hybrid steel trussed concrete beams (HSTCBs)." *J. Constr. Steel Res.*, 111, 88–102.
- Colajanni, P., La Mendola, L., Latour, M., Monaco, A., and Rizzano, G. (2017). "Analytical prediction of the shear connection capacity in precast steel-concrete trussed beams." *Mater. Struct.*, 50(1), 48.
- Colajanni, P., La Mendola, L., and Monaco, A. (2014). "Stress transfer mechanisms investigation in hybrid steel trussed-concrete beams by push-out tests." *J. Constr. Steel Res.*, 95, 56–70.
- Colajanni, P., La Mendola, L., and Monaco, A. (2015b). "Stiffness and strength of composite truss beam to R.C. column connection in MRFs." *J. Constr. Steel Res.*, 113, 86–100.
- Colajanni, P., La Mendola, L., and Monaco, A. (2016a). "Experimental investigation of the shear response of precast steel-concrete trussed beams." *J. Struct. Eng.*, 10.1061/(ASCE)ST.1943-541X.0001642, 04016156.
- Colajanni, P., La Mendola, L., Monaco, A., and Recupero, A. (2016b). "Validation of a shear model for RC and hybrid beams with two different inclinations of transversal reinforcement." *Appl. Mech. Mater.*, 847, 505–512.
- Colajanni, P., La Mendola, L., and Recupero, A. (2013). "Experimental test results vs. analytical prediction of welded joint strength in hybrid steel trussed concrete beams (HSTCBs)." *EJECE*, 17(8), 742–759.
- Eligehausen, R., Popov, E. P., and Bertero, V. V. (1983). "Local bond stress-slip relationships of deformed bars under generalized excitations." *Rep. No. UCB/EERC 83-23*, Univ. of California, Berkeley, CA.
- Hsu, H. L., Hsieh, J. C., and Juang, J. L. (2004). "Seismic performance of steel-encased composite members with strengthening cross-inclined bars." *J. Constr. Steel Res.*, 60(11), 1663–1679.
- Ju, Y. K., Kim, J. Y., and Kim, S. D. (2007). "Experimental evaluation of new concrete encased steel composite beam to steel column joint." *ASCE J. Struct. Eng.*, 10.1061/(ASCE)0733-9445(2007)133:4(519), 519–529.
- Lee, J., and Fenves, G. L. (1998). "Plastic-damage model for cyclic loading of concrete structures." *J. Eng. Mech.*, 10.1061/(ASCE)0733-9399(1998)124:8(892), 892–900.
- Lepech, M., and Li, V. C. (2003). "Preliminary findings on size effect in ECC structural members in flexural." *Proc., 7th Int. Symp. on Brittle Matrix Composites*, Woodhead Publishing Ltd., Cambridge, U.K., 57–66.
- Lepech, M., and Li, V. C. (2004). "Size effect in ECC structural members in flexure." *Proc., 5th Int. Conf. on Fracture Mechanics of Concrete and Concrete Structures (FraMCOS-5)*, Univ. of Michigan, Ann Arbor, MI, 1059–1066.
- Monaco, A. (2014). "Experimental analysis, numerical and analytical modeling of shear strength mechanisms in hybrid steel trussed concrete beams." Ph.D. thesis, Dept. of Civil, Environmental, Aerospace and Material Engineering, Univ. of Palermo, Palermo, Italy.
- Monaco, A. (2016). "Numerical prediction of the shear response of semi-prefabricated steel-concrete trussed beams." *Constr. Build. Mater.*, 124, 462–474.
- Monti, G., and Petrone, F. (2015). "Shear resisting mechanisms and capacity equations for composite truss beams." *J. Struct. Eng.*, 10.1061/(ASCE)ST.1943-541X.0001266, 04015052.
- Ožbolt, J., Eligehausen, R., and Petrangeli, M. (1994). *The size effect in concrete structures*, E&FN Spon, London.
- Sassone, M., and Chiorino, M. A. (2005). "Design aids for the evaluation of creep induced structural effects." *Shrinkage and creep of concrete*, J. Gardner and J. Weiss, eds., American Concrete Institute (ACI), Farmington Hills, MI, 239–259.
- Syroka-Korol, E., and Tejchman, J. (2012). "Numerical studies on size effects in concrete beams." *Archit. Civil Eng. Environ.*, 2, 67–78.
- Syroka-Korol, E., and Tejchman, J. (2013). "Experimental and numerical investigations of size effects in reinforced concrete beams with steel or basalt bars." *Proc., 8th Int. Conf. on Fracture Mechanics of Concrete and Concrete Structures (FraMCOS-8)*, International Center for Numerical Methods in Engineering, Barcelona, Spain, 10–14.
- Tesser, L., and Scotta, S. (2013). "Flexural and shear capacity of composite steel truss and concrete beams with inferior precast concrete base." *Eng. Struct.*, 49, 135–145.
- Trentadue, F., Quaranta, G., Marano, G. C., and Monti, G. (2011). "Simplified lateral-torsional buckling analysis in special truss-

- reinforced composite steel-concrete beams." *J. Struct. Eng.*, 10.1061/(ASCE)ST.1943-541X.0000390, 1419–1427.
- Tullini, N., and Minghini, F. (2013). "Nonlinear analysis of composite beams with concrete-encased steel truss." *J. Constr. Steel Res.*, 91, 1–13.
- Vincenzi, L., and Savoia, M. (2010). "Stabilità di tralicci PREM in prima fase [Stability of PREM-beams in the first phase]." *Proc., 18th Collegio Tecnici industrializzazione Edilizia (CTE) Congress*, Laser Copy Center, Milano, Italy, 849–858 (in Italian).
- Yasir Alam, S., and Loukili, A. (2010). "Application of digital image correlation to size effect tests of concrete." *Proc., 7th Int. Conf. on Fracture Mechanics of Concrete and Concrete Structures (FraMCoS-7)*, B. H. Oh, et al., eds., Korea Concrete Institute, Seoul.
- Yu, Q., Le, J.-L., Hubler, M., Wendner, R., Cusatis, G., and Bažant, Z. P. (2016). "Comparison of main models for size effect on shear strength of reinforced or prestressed concrete beams." *Struct. Concr.*, 17(5), 778–789.